

Numerical Simulation of the Performance of Single Qubit Gates for Trapped Ions

L. A. Akopyan^{a,*}, O. Lakhmanskaya^a, S. Yu. Zarutskiy^a, N. D. Korolev^a,
O. Guseva^a, and K. Lakhmanskiy^{a,b}

^a Russian Quantum Center, Skolkovo, Moscow, 143025 Russia

^b Higher School of Systems Engineering, Moscow Institute of Physics and Technology (National Research University),
Dolgoprudnyi, Moscow region, 141701 Russia

*e-mail: l.akopyan@rqc.ru

Received September 2, 2022; revised September 2, 2022; accepted September 15, 2022

Finite gate errors limit performance of modern quantum computers. In this work, we study single qubit gate fidelities for trapped ions. For this we have numerically solved Schrödinger equation using full Hamiltonian of the system for one, two, three and four ions. This approach allows us to analyze gate errors beyond the LambDicke approximation and to take into account not only a finite occupation of the phonon modes, but also the effects related to the ion–phonon entanglement. As a result, we show how infidelity of the global single qubit gates depend on the initial phonon mode occupations, the Lamb–Dicke parameter, Rabi frequency and the number of ions.

DOI: 10.1134/S0021364022601956

1. INTRODUCTION

Quantum computing with trapped ions has shown significant progress over the last couple of decades [1–5]. The main advantages are the highest-fidelity quantum computing gates, long coherence times, inherent uniformity and all-to-all connectivity [6–11]. Nowadays the attention has shifted from miniature architectures towards more practical implementations requiring to scale up the computer performance [12–19]. Scaling does not only mean having more qubits but also having the ability to control and measure a large number of ions, to keep high performance of gates achieved in the few-ion proof-of-principle systems independent on the number of qubits or the number of required operations [20], [21]. Overall, system performance is known to degrade for large ion crystals [1]. Therefore, it is crucial to understand scaling of finite errors in quantum gates with the system size due to noise, decoherence, and control imperfections.

The dynamics of single-qubit gates in trapped-ion systems is typically described using Lamb–Dicke approximation meaning the exclusion of the phonon modes [2, 7, 22]. The leading term contribution of this approximation does not contain the phonon modes, whereas the second one scales as $\eta^2 \Omega n$. Here η is the Lamb–Dicke parameter, Ω is the Rabi frequency, n is the occupation of the phonon mode. Given finite heating rates in experiments the importance of the second term increases as the time elapses. Fault toler-

ant quantum computations require infidelities ranging from 10^{-2} to 10^{-4} [23–25]. This becomes crucial for long gate sequences required by quantum algorithms, because every next gate will have worse fidelity.

Here we present systematic analysis on the dependence of the single qubit gate fidelities on the occupation of the phonon modes beyond Lamb–Dicke approximation. In particular, we consider optical Calcium ion qubit and perform numerical simulation of the action of the gate $R_\phi(\theta)$ usually described as the following unitary operation [2], [7]:

$$R_\phi(\theta) = \begin{pmatrix} \cos\left(\frac{\theta}{2}\right) & -ie^{-i\phi} \sin\left(\frac{\theta}{2}\right) \\ -ie^{i\phi} \sin\left(\frac{\theta}{2}\right) & \cos\left(\frac{\theta}{2}\right) \end{pmatrix}, \quad (1)$$

where ϕ is the phase of the laser, and angle $\theta = \tau\Omega$ is controlled via the gate time τ . We focus on such parameters as the different numbers of ions (up to 4 ions in the chain), the phonon mode occupation, the strength of the Lamb–Dicke parameter and the gate time.

The paper is organized as follows. Section 2 contains the description of the considered trapped ions single qubit gates and Hamiltonian of the problem. Section 3 gives details of simulation methods used to calculate gate fidelity. Results and conclusions are presented in Section 4, 5.

2. SYSTEM HAMILTONIAN

To take into account gate errors coming from the phonon mode excitations and finite values of the Lamb–Dicke parameter, we use the full Hamiltonian of a chain of N equal ions in a linear Paul trap potential. It consists of electronic (qubit) part, motional part and atom–light interaction:

$$\hat{H}_N = \sum_{p=1}^N \hbar \frac{\omega_q}{2} \hat{\sigma}_z^p + \sum_j \sum_{k=1}^N \hbar \omega_{jk} \left(\hat{a}_{jk}^\dagger \hat{a}_{jk} + \frac{1}{2} \right) + \frac{\hbar}{2} \sum_{p=1}^N \Omega \left[e^{-i(\omega t - \mathbf{k} \hat{\mathbf{R}}_p + \phi)} \hat{\sigma}_p^+ + \text{h.c.} \right]. \quad (2)$$

Here, indices p and j refer to the ion index in the chain and to the choice of the Cartesian axis (x, y, z), respectively, ω_q is the qubit transition frequency, ω is the laser frequency, ω_{jk} is the frequency of the normal mode k along axis j , $\hat{a}_{jk}^\dagger/\hat{a}_{jk}$ are creation/annihilation operators of the normal mode k along axis j , k is the wave vector of the laser, $\hat{\mathbf{R}}_p$ is the quantized coordinate of the center of mass of ion p . The product $\mathbf{k} \hat{\mathbf{R}}_p$ gives characteristic ion–phonon interaction strength called the Lamb–Dicke parameter, responsible for population leakage from ion states to the phonon states. We assume the ideal harmonic potential of the trap and disregard micromotion coming from the dynamics of the ions inside the Paul trap. Therefore, the spectrum of normal modes depends only on the axial ω_a and the radial ω_r trap secular frequencies, and the motional part is represented by a set of independent phonon modes described as quantized oscillators. The laser–ion interaction part in (2) is responsible for the interaction between the qubits and the phonon modes and is considered in the rotating wave approximation. In the frame of the normal mode description of motion the coordinate of the ion is expanded in the following way [26, 27]:

$$\hat{\mathbf{R}}_{pj} = R_{pj}^0 \hat{\mathbb{1}} + \sum_{k=1}^N S_{pj k} \sqrt{\frac{\hbar}{2m\omega_{jk}}} (\hat{a}_{jk} + \hat{a}_{jk}^\dagger). \quad (3)$$

Here, R_{pj}^0 denotes ion equilibrium positions, $\hat{\mathbb{1}}$ is the phonon modes identity operator, m is the mass of the ion, $S_{pj k}$ is the matrix-element of transition matrix S from the ion coordinates to the phonon modes, and the Lamb–Dicke parameter $\eta_{pj k}$ is defined as follows:

$$\eta_{pj k} = k_j S_{pj k} \sqrt{\frac{\hbar}{2m\omega_{jk}}}, \quad (4)$$

standard derivation of the action of $R_q(\theta)$ gate assumes that the phonon modes state does not change during the gate operation [2, 7]. Given small values of the Lamb–Dicke parameter, the exponential operator

$\exp(i\mathbf{k} \hat{\mathbf{R}}_p)$ in \hat{H}_N (2) can be expanded with respect to $\eta_{pj k} (\hat{a}_{jk} + \hat{a}_{jk}^\dagger)$.

To take into account the finite phonon mode occupation numbers, the second order of this expansion can be included in Eq. (1) as a correction to the Rabi frequency, as follows (up to the second order, for higher orders see [28]):

$$\Omega_p = \Omega \left(1 - \sum_j \sum_{k=1}^N \eta_{pj k}^2 (n_{kj} + 1/2) \right), \quad (5)$$

where n_{kj} is the occupation number of mode k along axis j . Numerical simulations allow us to make step forward and to take into account not only heating effects, but also the effects related to ions-to-mode and inter-ion entanglement. They occur because of the changes in the phonon mode occupations during gate operation and come from the expansion terms not included in corrections to the Rabi frequency (5). To study these effects, we numerically integrate the Schrödinger equation for ion–phonon wavefunction with Hamiltonian (2) and compute gate fidelities as functions of time for different experimental parameters (see Section 4). The numerical simulations are performed with QuantumOptics.jl package [29] of Julia language [30].

3. CALCULATION OF FIDELITY

In this work we consider only globally addressed single qubit gates along the chain (see Fig. 1), and imply that only axial phonon modes influence the ion chain dynamics via Eq. (2). We present the initial ion–phonon wavefunction in the form of a tensor product of the N axial phonons and N qubits:

$$|\psi(0)\rangle = |n_1 n_2 \dots n_N\rangle |\psi_1 \psi_2 \dots \psi_N\rangle, \quad (6)$$

where $|n_k\rangle$ is a Fock state with n_k phonons in the axial phonon mode k , $|\psi_p\rangle$ is the initial wavefunction for a qubit p . We present all the qubit initial states as the ground state of the qubit.

To compute the fidelity of the $R_q(\theta)$ gate, at first, we find the wavefunction $|\psi_{\text{ideal}}\rangle = \hat{U}_{\text{ideal}} |\psi(0)\rangle$ obtained after the action of the ideal operator:

$$\hat{U}_{\text{ideal}} = \hat{U}_{\text{osc}}^1 \otimes \dots \otimes \hat{U}_{\text{osc}}^N \otimes \hat{R}_q(\theta) \otimes \dots \otimes \hat{R}_q(\theta), \quad (7)$$

where $\hat{U}_{\text{osc}}^k = \exp\left\{-\frac{i}{\hbar} \hat{H}_{\text{osc}}^k \theta\right\}$ is evolution operator with axial phonon Hamiltonian $\hat{H}_{\text{osc}}^k = \hbar \omega_k \left(a_k^\dagger a_k + \frac{1}{2} \right)$ describing the free evolution of an oscillator. Second, the wavefunction $|\psi_{\text{final}}\rangle$ is obtained under evolution with the full Hamiltonian (2):

$$|\psi_{\text{final}}\rangle = \exp\left\{-\frac{i}{\hbar} \hat{H}_N t\right\} |\psi(0)\rangle. \quad (8)$$

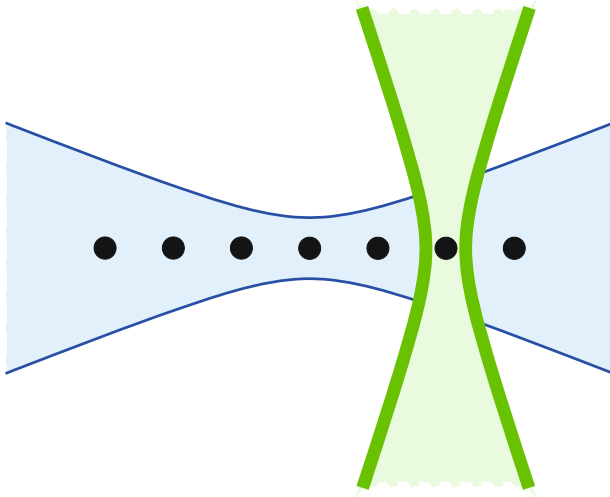


Fig. 1. (Color online) Individual and global addressing of a chain of trapped ions in a Paul trap.

Finally, the fidelity is calculated via projection of the final state wavefunction onto the ideal state of the phonons and the qubits $|\psi_{\text{ideal}}\rangle$. Computed fidelities depend on the initial state of the phonon-ion system and the gate duration.

We distinguish two types of fidelities \mathcal{F} and F , determined in the following way:

$$\mathcal{F}(\psi_{\text{final}}, \psi_{\text{ideal}}) = \langle \psi_{\text{ideal}}^{\text{qubit}} | \hat{\rho}_{\text{final}}^{\text{qubit}} | \psi_{\text{ideal}}^{\text{qubit}} \rangle, \quad (9)$$

$$\hat{\rho}_{\text{final}}^{\text{qubit}} = \text{Tr}_{\text{phonons}} [|\psi_{\text{final}}\rangle \langle \psi_{\text{final}}|],$$

$$|\psi_{\text{ideal}}^{\text{qubit}}\rangle = \hat{R}_\phi(\theta) \otimes \dots \otimes \hat{R}_\phi(\theta) |\psi_1 \psi_2 \dots \psi_N\rangle, \quad (10)$$

$$F = \langle \psi_{\text{ideal}} | \psi_{\text{final}} \rangle^2.$$

Function \mathcal{F} corresponds to the measurement in which the states of the phonon modes cannot be resolved, whereas F implies that the phonon modes can also be measured. In particular, \mathcal{F} is calculated with tracing out the phonon modes and projecting the final qubit state on the ideal one. The function F includes the phonons in the ideal state via projecting the final phonon-qubit wavefunction onto the ideal one.

Comparison of these two types of fidelities allows one to quantify the entanglement between ions and modes. In the next section we show the results of our analysis and compare these two functions for fidelity calculation. To verify the existence of an entanglement we also compute the von Neumann entanglement entropy between ions and phonon modes according to the following formula:

$$S_{\text{ent}} = -\text{Tr} [\hat{\rho}_{\text{final}}^{\text{qubit}} \log (\hat{\rho}_{\text{final}}^{\text{qubit}})]. \quad (11)$$

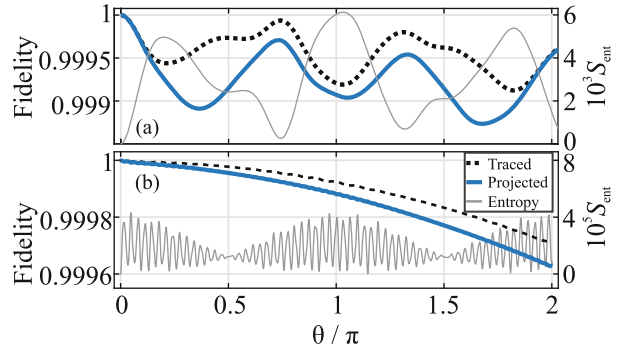


Fig. 2. (Color online) Computed fidelities of the single-qubit gates (top panel) G_1 and (bottom panel) G_{15} versus the angle θ . The results were obtained for three ions for zero initial phonon mode occupations. The dotted line represents the fidelity \mathcal{F} , when the phonon modes are traced. The thick solid line represents the projected fidelity F . The thin solid line shows the entanglement entropy S_{ent} between all phonon modes and ions.

4. RESULTS AND DISCUSSION.

In this work we consider gates with two different magnitudes of Rabi frequencies referring to them as gates G_1 and G_{15} . The chosen values of Ω correspond to the $\pi/2$ pulse duration of 1 μs (G_1) and 15 μs (G_{15}). Another simulation parameters are the axial secular frequencies, which affect the normal frequencies and, hence, the Lamb–Dicke parameters. The values of the axial secular frequencies are taken from the experimental works [2, 7] and are equal to $2\pi \cdot 1$ MHz unless otherwise stated.

First, we study the difference between the two types of fidelities \mathcal{F} and F . For that, we assume the absence of the phonons in the system and compute \mathcal{F} and F for a chain of 3 ions as shown in Fig. 2. The two panels refer to the gates G_1 and G_{15} , and qualitatively show that fidelities \mathcal{F} and F differ from each other. This difference indicates that the states of the ions and the phonon modes got entangled during the gate operation. To verify this, we compute the entanglement entropy between ions and phonons and, indeed, see that the extrema of the entanglement entropy coincide with the oscillations of the traced fidelity (see upper panel in Fig. 2).

The oscillations are also present in the case of the slow gate G_{15} , but their amplitude is much smaller, as the amplitude of the entanglement entropy oscillations. Comparison of the two panels in Fig. 2 also shows that the magnitude of the gate error and the amplitude of the fidelity oscillations increase with the gate speed. The difference between the two types of fidelities does not exceed 6×10^{-4} . Further we use only projected fidelities as in numerical simulations we can accurately take into account the phonon modes and their occupations.

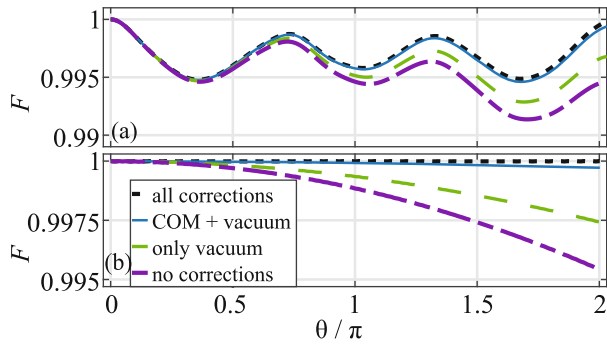


Fig. 3. (Color online) Computed fidelities of the single-qubit gates (top panel) G_1 and (bottom panel) G_{15} versus the angle θ . The initial state of phonon modes is $|n_{\text{COM}}n_2n_3\rangle = |211\rangle$. Different line styles distinguish different cases depending on how the ideal gate operation was simulated: using corrections for the Rabi frequency (the colored lines except the dash-dotted one) from Eq. (5) or without the corrections (dash-dotted line). The number of modes/phonons taken into account for the corrections is specified in the legend.

Now we will focus on the understanding of the mechanisms responsible for the gate errors: heating, entanglement, or both. For this we compute the gate fidelities F by projecting the final state $|\psi_{\text{final}}\rangle$ onto the modified ideal state calculated with corrected Rabi frequencies (see Eq. (5)). Corrected Ω includes only heating effects. We did the simulations for three ions, for the initial phonon mode occupation $|n_{\text{COM}}n_2n_3\rangle = |211\rangle$, and for the cases listed below:

- (1) no corrections are taken into account;
- (2) only vacuum corrections are included; i.e., the Rabi frequency in ideal gate is changed according to Eq. (5) with $n_k = 0$ (this calculation requires only the knowledge of the normal mode frequencies);
- (3) only the occupation of the center of mass (COM) mode and the vacuum corrections are included; i.e., the Rabi frequency in ideal gate is changed according to Eq. (5) with the phonon mode

occupation $|n_{\text{COM}}n_2n_3\rangle = |200\rangle$ (requires the knowledge of the normal frequencies and the COM mode occupation number);

(4) all the corrections are taken into account; i.e., all the corresponding n_k are included into Eq. (5) (this implies the knowledge about all the normal frequencies and the occupation numbers).

The results are shown in Fig. 3. One can see that fidelity improves significantly, when corrections to the Rabi frequency are included. The main contribution comes from the COM mode. In fact, it is comparable with the case when all the corrections are included. Importantly, the latter holds if initial COM mode occupation is greater or equal to the initial occupation of any other mode. The minimum infidelity of 10^{-4} is achieved for the gate G_{15} , when the corrections for all the modes are included. For the fast G_1 gate the situation is worse: the oscillations of fidelity cannot be removed by correcting the Rabi frequency. As it was mentioned above, these oscillations come from the entanglement between the phonon modes and the ions. Contrary, the envelope characterizing the degradation of the gate over its duration is attributed to the occupation of the phonon modes and, in fact, can be compensated using Eq. (5).

Further we explore the impact of the finite initial phonon mode occupation on the gate fidelity F and the amplitude of their oscillation. The results of the numerical simulations for three ions and for the gates G_1 and G_{15} are shown in Fig. 4. Overall, an increase in the phonon mode occupation leads to a more rapid decrease in the fidelity. The amplitude of the oscillations again scales with Ω . It also increases with the phonon mode occupation number. The largest contribution to the infidelity and to the amplitude of its oscillation comes from the population of the COM mode similar to the Fig. 3. We associate this fact with the magnitude of Lamb–Dicke parameter, which is the largest for the COM mode.

To confirm this, we study the dependence of the fidelity on the Lamb–Dicke parameter for the initial

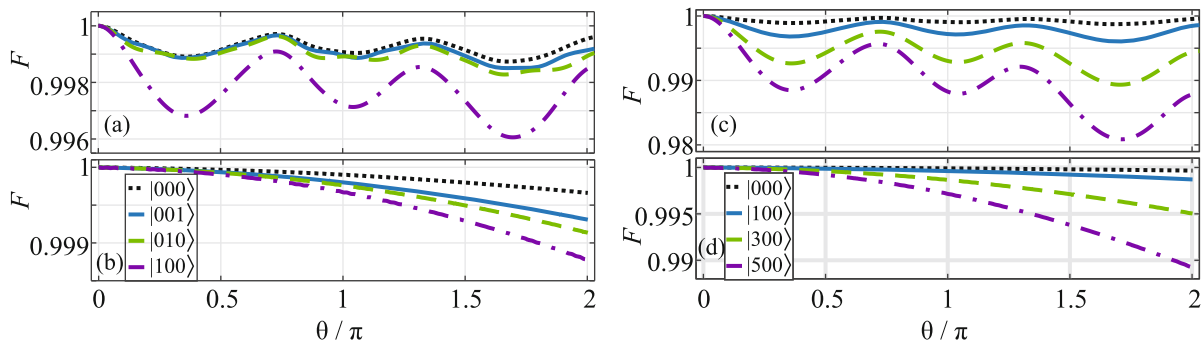


Fig. 4. (Color online) Computed fidelities of single-qubit gates (top panels) G_1 and (bottom panels) G_{15} for three ions versus the gate time expressed in units of θ/π . The line styles distinguish different mode occupations depicted in the legend as $|n_{\text{COM}}n_2n_3\rangle$.

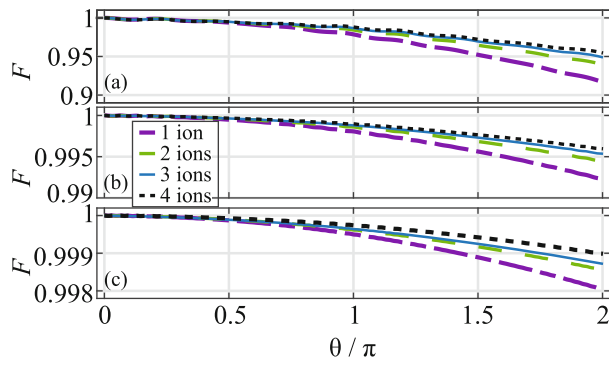


Fig. 5. (Color online) Computed fidelities of single-qubit gates G_{15} versus the angle θ and initial phonon state taken as one phonon in the COM-mode and no phonons in all the other modes. Line styles correspond to the different numbers of ions specified in the legend: (a) $\eta \approx 0.25$ for one ion (corresponds to the axial secular frequency $\omega_a = 2\pi \times 0.15$ MHz), (b) $\eta \approx 0.14$ for one ion (corresponds to the axial secular frequency $\omega_a = 2\pi \times 0.5$ MHz), and (c) $\eta \approx 0.1$ for one ion (corresponds to the axial secular frequency $\omega_a = 2\pi \times 1.0$ MHz).

phonon mode state $|100\rangle$ corresponding to a single phonon in a COM mode. Since η scales down with the square root of the number of ions ($N = [1-4]$) and the axial secular frequency, we modified those parameters. The results are summarized in Fig. 5. The axial secular frequency ω_a was chosen from the range $2\pi[0.15, 0.5, 1.0]$ taken from [7, 2]. Indeed, we observe less profound decrease in the fidelity as the ion chain gets longer and for the larger axial frequencies.

5. CONCLUSIONS

In this work we have studied the performance of global single-qubit gates depending on the Lamb–Dicke parameter, gate time, the number of ions, and the initial phonon mode occupation numbers. We have performed numerical simulation of the action of the $R_\phi(\theta)$ gate using full Hamiltonian of the system (2). This allows us to take into account the two effects responsible for gate errors: entanglement between the qubit states and the phonon modes and phonon mode heating which leads to the finite occupation of the phonon modes. Qualitatively, the gate fidelities improve for slower gates (small Rabi frequency Ω) and small Lamb–Dicke parameter η . For the slow gates (e.g., $\pi/2$ pulse duration is of 15 μs), the gate performance can be well characterized with modified Rabi frequency using Eq. (5), whereas for gates as fast as G_1 (the $\pi/2$ pulse duration is 1 μs) numerical simulations are required to include the entanglement effects. In particular, we observe the oscillatory time dependence of the gate performance which cannot be taken into account solely using corrections to the Rabi frequency

according to Eq. (5). This oscillatory effect originates from the ion–phonon entanglement. Its period and amplitude scale with the Rabi frequency Ω , the Lamb–Dicke parameter η and the phonon mode occupation number.

The developed software package will be used to optimize single-qubit gate parameters for experimental setup handling trapped ions and will be also extended for mixed species chains. The results and analyses will be useful for error mitigation in quantum algorithms performed on ions, optimization of long gate sequences as well as the development of new variational algorithms taking into account present error models.

ACKNOWLEDGMENTS

We are grateful to E. Anikin, A. Matveev, and M. Popov for fruitful discussions.

FUNDING

This work was supported by Rosatom (contract no. 868-1.3-15/15-2021 dated October 5, 2021, Roadmap for Quantum Computing).

CONFLICT OF INTEREST

The authors declare that they have no conflicts of interest.

OPEN ACCESS

This article is licensed under a Creative Commons Attribution 4.0 International License, which permits use, sharing, adaptation, distribution and reproduction in any medium or format, as long as you give appropriate credit to the original author(s) and the source, provide a link to the Creative Commons license, and indicate if changes were made. The images or other third party material in this article are included in the article’s Creative Commons license, unless indicated otherwise in a credit line to the material. If material is not included in the article’s Creative Commons license and your intended use is not permitted by statutory regulation or exceeds the permitted use, you will need to obtain permission directly from the copyright holder. To view a copy of this license, visit <http://creativecommons.org/licenses/by/4.0/>.

REFERENCES

1. C. D. Bruzewicz, J. Chiaverini, R. McConnell, and J. M. Sage, *Appl. Phys. Rev.* **6**, 021314 (2019).
2. I. Pogorelov, T. Feldker, Ch. D. Marciniak, L. Postler, G. Jacob, O. Kriegelsteiner, V. Podlesnic, M. Meth, V. Negnevitsky, M. Stadler, B. Höfer, C. Wächter, K. Lakhmanskiy, R. Blatt, P. Schindler, and T. Monz, *PRX Quantum* **2**, 1 (2021).
3. C. Monroe, W. C. Campbell, L.-M. Duan, Z.-X. Gong, A. V. Gorshkov, P. W. Hess, R. Islam, K. Kim, N. M. Linke, G. Pagano, P. Richerme, C. Senko, and N. Y. Yao, *Rev. Mod. Phys.* **93** (2021).

4. M. Ringbauer, M. Meth, L. Postler, R. Stricker, R. Blatt, P. Schindler, and T. Monz, *Nat. Phys.* **18**, 1053 (2022).
5. K. Wright, K. Beck, S. Debnath, et al., *Nat. Commun.* **10**, 1 (2019).
6. P. Zoller and J. I. Cirac, *Phys. Rev. Lett.* **74**, 1 (1995).
7. P. Schindler, D. Nigg, T. Monz, J. T. Barreiro, E. Martinez, S. X. Wang, S. Quint, M. F. Brandl, V. Nebendahl, and C. F. Roos, *New J. Phys.* **15**, 123012 (2013).
8. M. A. Nielsen and I. L. Chuang, *Quantum Computation and Quantum Information*, 10 ed. (Cambridge Univ. Press, Cambridge, 2010).
9. H. Häffner, C. Roos, and R. Blatt, *Phys. Rep.* **469**, 155 (2008).
10. R. Blatt and D. Wineland, *Nature (London, U.K.)* **453**, 1008 (2008).
11. T. P. Harty, D. T. C. Allcock, C. J. Ballance, L. Guidoni, H. A. Janacek, N. M. Linke, D. N. Stacey, and D. M. Lucas, *Phys. Rev. Lett.* **113**, 2 (2014).
12. F. Arute, K. Arya, R. Babbush, et al., *Nature (London, U.K.)* **574**, 505 (2019).
13. J. Zhang, G. Pagano, P. W. Hess, A. Kyprianidis, P. Becker, H. Kaplan, A. V. Gorshkov, Z.-X. Gong, and C. Monroe, *Nature (London, U.K.)* **551**, 601 (2017).
14. J. Benhelm, G. Kirchmair, C. F. Roos, and R. Blatt, *Nat. Phys.* **4**, 463 (2008).
15. T. Monz, D. Nigg, E. A. Martinez, M. F. Brandl, P. Schindler, R. Rines, S. X. Wang, I. L. Chuang, and R. Blatt, *Science (Washington, DC, U. S.)* **351**, 1068 (2016).
16. C. Figgatt, A. Ostrander, N. M. Linke, K. A. Landsman, D. Zhu, D. Maslov, and C. Monroe, *Nature (London, U.K.)* **572**, 368 (2019).
17. C. Hempel, C. Maier, J. Romero, J. McClean, T. Monz, H. Shen, P. Jurcevic, B. P. Lanyon, P. Love, R. Babbush, A. Aspuru-Guzik, R. Blatt, and C. F. Roos, *Phys. Rev. X* **8**, 031022 (2018).
18. K. K. Mehta, C. Zhang, M. Malinowski, T. L. Nguyen, M. Stadler, and J. P. Home, *Nature (London, U.K.)* **586**, 533 (2020).
19. R. J. Niffenegger, J. Stuart, C. Sorace-Agaskar, D. Kharras, S. Bramhavar, C. D. Bruzewicz, W. Loh, R. T. Maxson, R. McConnell, D. Reens, G. N. West, J. M. Sage, and J. Chiaverini, *Nature (London, U.K.)* **586**, 538 (2020).
20. A. Crippa, R. Ezzouch, A. Aprá, A. Amisse, R. Laviéville, L. Hutin, B. Bertrand, M. Vinet, M. Urdampilleta, T. Meunier, M. Sanquer, X. Jehl, R. Maurant, and S. de Franceschi, *Nat. Commun.* **10**, 2776 (2019).
21. M. C. Jarratt, S. J. Waddy, A. Jouan, A. C. Mahoney, G. C. Gardner, S. Fallahi, M. J. Manfra, and D. J. Reilly, *Phys. Rev. Appl.* **14**, 064021 (2020).
22. D. Leibfried, R. Blatt, C. Monroe, and D. Wineland, *Rev. Mod. Phys.* **75**, 281 (2003).
23. A. M. Steane, *Phys. Rev. A* **68**, 042322 (2003).
24. B. W. Reichardt, arXiv: quant-ph/0612004 (2006).
25. E. Knill, *Nature (London, U.K.)* **434**, 39 (2005).
26. D. F. V. James, *Appl. Phys. B* **66**, 181 (1998).
27. J. P. Home, arXiv: 1306.5950 (2013).
28. N. Semenina, A. S. Borisenko, V. Zalivako, I. A. Semerikov, M. D. Aksenov, K. Yu. Khabarova, and N. N. Kolachevsky, *JETP Lett.* **116**, 75 (2022).
29. S. Krämer, D. Plankensteiner, L. Ostermann, and H. Ritsch, *Comput. Phys. Commun.* **227**, 109 (2018).
30. J. Bezanson, A. Edelman, S. Karpinski, and V. B. Shah, *SIAM Rev.* **59**, 65 (2017).